Hierarchical superhydrophilic/superaerophobic 3D porous trimetallic (Fe, Co, Ni) spinel/carbon/nickel foam for boosting oxygen evolution reaction

Liang Ma [a,b], Zengyan Wei [a,*], Chen Zhao [a,b], Xiangyu Meng [a,b], Honglei Zhang [a,b], Meixiu Song [a,b], Yaming Wang [a,b], Baoqiang Li [a,b], Xiaoxiao Huang [a,b], Chengyan Xu [c], Ming Feng [d], Peigang He [a,b], Dechang Jia [a,b,**], Yu Zhou [a,b], Xiaoming Duan [a,b,**]

[a] *Key Laboratory of Advanced Structural-Functional Integration Materials & Green Manufacturing Technology, Harbin Institute of Technology, Harbin 150001, China*
[b] *Institute for Advanced Ceramics, School of Materials Science and Engineering, Harbin Institute of Technology, Harbin 150001, China*
[c] *School of Materials Science and Engineering, and MOE Key Laboratory of Micro-Systems and Micro-Structures Manufacturing, Harbin Institute of Technology, Harbin 150001, China*
[d] *Key Laboratory of Functional Materials Physics and Chemistry of the Ministry of Education, Jilin Normal University, Changchun 130103, China*

ARTICLE INFO

ABSTRACT

Commercial oxygen evolution reaction catalysts are required operation under high current density to achieve rapid gas generation during electrochemical water splitting; however, oxygen bubbles readily cover active surfaces of electrodes, impeding reaction kinetics. Here, we introduce a facile, low-cost, and easy large-scale preparation strategy to synthesize trimetallic (Fe, Co, Ni) spinel/carbon/nickel foam (FeCoNiO$_x$/C/NF) electrodes with 3D network structures, and demonstrate that oxygen bubbles can be rapidly removed from the surface of electrodes with superhydrophilic/superaerophobic properties. The resulting FeCoNiO$_x$/C/NF electrodes exhibit a low overpotential of 221 mV with extremely low Tafel slope of 21 mV dec^{-1} at a current density of 10 mA cm^{-2} in 1 M KOH. At a high current density of 500 mA cm^{-2}, FeCoNiO$_x$/C/NF electrodes show a low overpotential of 325 mV with long-term stability for 250 h.

1. Introduction

The rapid depletion of fossil fuels has stimulated extensive research interest in seeking sustainable and environment-friendly energy conversion and storage systems [1]. One of the key solutions is to develop electrochemical water splitting (EWS, 2 H$_2$O → 2 H$_2$ + O$_2$) technology for clean hydrogen production, which can be coupled with intermittent renewable electricity [2–8]. Nevertheless, the application of EWS is restricted by the sluggish kinetics of oxygen evolution reaction (OER), where the rate-limiting step involves a complex four proton and four electron coupled transfer process with high energy barriers [9–12]. Furthermore, under an industrial-level OER scenario, EWS should be conducted at high current densities ($\geq$ 500 mA cm^{-2}) [12–14]. However, oxygen (O$_2$) bubbles are readily aggregated at the interface between the electrode and electrolyte. The bubbles can cover active sites, destruct electrode structures and hinder mass transport, leading to

inferior electrocatalytic activity and stability [15–17]. In an effort to achieve high current density in conjunction with maintaining its durability, O$_2$ bubbles must be rapidly removed from the electrode after generation [18]. To this end, it is critical to endow electrodes with extreme wettability and gas bubble-repellent function [15]. Due to the discontinuity of the three-phase interface (electrolyte, electrode, and O$_2$), bubbles are easily broken away from superaerophobic/superhydrophilic surfaces when their volumes are tiny [19]. Following this concept, electrocatalysts including woodpile-structured Ir [20], Ni$_2$P nanoarray [17], karst-featured Ni(0)@Ni(II) [18], nano-needle/microflower Ce$_x$Co$_{3-x}$O$_4$ cluster [21], core-shell structured Ni$_2$Co$_1$@Ni$_2$Co$_1$O$_x$ [22], NiSe$_2$/NiFe$_2$Se$_4$ nanowrinkles [23], Co-CH@NiFe-LDH/NF [24] were fabricated. However, a critical drawback exists in that the preparation involves complex procedures and harsh conditions. As such, it is difficult to scale up for the practical application [15].

---

* Corresponding author.
** Corresponding authors at: Key Laboratory of Advanced Structural-Functional Integration Materials & Green Manufacturing Technology, Harbin Institute of Technology, Harbin 150001, China.
E-mail addresses: zwei@hit.edu.cn (Z. Wei), dcjia@hit.edu.cn (D. Jia), dxmhit@126.com (X. Duan).

Recently, Bae et al. reported a simple method to prepare super-aerophobic materials. Through coating three-dimensional (3D) network polyethyleneimine (PEI) hydrogels on bare nickel foam (NF), the resulting electrode materials demonstrate excellent electrochemical performance for hydrogen evolution reaction (HER) [16]. Nevertheless, PEI hydrogels are inert materials that have no electrocatalytic activity in EWS, and the hydrophilicity properties of electrodes are not studied. Inspired by their method, we prepare trimetallic (Fe, Co, Ni) spinel/carbon/NF ($FeCoNiO_x$/C/NF) with 3D network structures as OER catalysts, and investigate the effect of super-aerophobic/superhydrophilic properties on the electrochemical performance in this study.

Noble metal-based materials, including IrO_2 and RuO_2, have demonstrated as the state-of-the-art catalysts for the energetic OER kinetics. Nevertheless, their scarcity, high cost, and poor long-term stability limit the industry-scale applications [2,25]. It is desirable to prepare cost-effective, stable, and high-performance non-noble metal electrocatalysts for industrial-level OER application [26,27]. Spinel-type oxides of the general formulation AB_2O_4 with competitive activity which has been extensively studied as a replacement to noble metal-based catalysts [28,29]. Among them, $NiCo_2O_4$ is of particular interest due to high activity, corrosion resistance, easy availability, and acceptable electrical conductivity [28,30]. Furthermore, recent study shows that Fe-doping can further enhance the activity of Ni^{2+} and Co^{2+} based OER electrocatalysts [31].

Herein, we prepare $FeCoNiO_x$/C/NF electrocatalysts with 3D network structures for OER via a facile impregnation-foaming-calcination strategy at relative low temperature. The 3D network structures provide high specific surface area and interconnected electron transfer access [11,32,33]. In addition, the resulting electrodes demonstrate superhydrophilic/superaerophobic properties, facilitating O_2 bubbles detachment during EWS. FeCoNi/C/NF electrocatalysts display exceptional performances at both a low and a high current density. In addition, they show robust durability with long-term stability for 250 h in alkaline solutions. This work provides rational design and large-scale synthesis of low cost electrocatalysts for EWS that can meet the industrial-level requirement of high current densities.

2. Experimental section

2.1. Materials

Chitosan (degree of deacetylation $\geq$ 95 %, viscosity: 100–200 mPa s), nickel(II) nitrate hexahydrate ($Ni(NO_3)_2$ 6 H_2O), cobalt(II) nitrate hexahydrate ($Co(NO_3)_2$ $6H_2O$) and iron(III) nitrate nonahydrate ($Fe(NO_3)_2$ $9H_2O$) were purchased from Macklin Chemical Reagent Co., Ltd (Shanghai, China). Nickel foam (NF, thickness: 1.5 mm) was purchased from Kunshan Anshu Material Co., Ltd. Potassium hydroxide (KOH), ethanol and glacial acetic acid was purchased from FuGuang Chemical Reagent Co. Ltd. (Tianjin, China). Nafion solution (5 wt %) was purchased from Sigma-Aldrich. RuO_2 was obtained from Suzhou Sinero Technology Co., Ltd. All reagents were of analytical grade.

2.2. Synthesis of Fe, Co, Ni, FeCo, CoNi, FeNi and FeCoNi-Chitosan gels

In a typical synthesis of FeCoNi-chitosan gels, $Fe(NO_3)_2$ $9H_2O$ (16 mmol), $Co(NO_3)_2$ $6H_2O$ (32 mmol), $Ni(NO_3)_2$ $6H_2O$ (16 mmol), chitosan (1.5 g) and 50 mL deionized water were added into a beaker. Then, 1 mL glacial acetic acid was added under stirring at 90 °C until a uniform gel was formed. For other gels, the feed ratios of Fe:Co:Ni were changed (Fe-chitosan gel = 1:0:0, Co-chitosan gel = 0:1:0, Ni-chitosan gel = 0:0:1, FeCo-chitosan gel = 1:2:0, CoNi-chitosan gel = 0:2:1, and FeNi-chitosan gel = 1:0:1) while keeping the total molar amount of metal at 64 mmol.

2.3. Synthesis of C/NF, FeO_x/C/NF, CoO_x/C/NF, NiO_x/C/NF, $FeCoO_x$/C/NF, $CoNiO_x$/C/NF, $FeNiO_x$/C/NF and $FeCoNiO_x$/C/NF electrocatalysts

OER electrocatalysts were prepared using an impregnation-foaming-calcination method. NF (cut into an area of 1 cm × 2 cm) was firstly cleaned successfully by diluted hydrochloric acid, ethanol and deionized water. In a typical synthesis of $FeCoNiO_x$/C/NF electrocatalysts, NF was impregnated into the as-prepared FeCoNi-gel, and dried for 6 h at 80 °C. The gel underwent a foaming process during the drying process accompanied by continuous volatilization of water vapor. Afterwards, the sample was calcined for 2 h at 300 °C with a ramping rate of 5 °C min^{-1} in argon atmosphere [34]. For preparing electrodes with other composition, one only needs to change the composition of gels. Subsequently, powder samples including FeO_x/C, CoO_x/C, NiO_x/C, $FeCoO_x$/C, $FeNiO_x$/C, $CoNiO_x$/C, and $FeCoNiO_x$/C were obtained via scrapping off NF.

2.4. Materials characterizations

Scanning electron microscopy (SEM) and energy-dispersive X-ray spectroscopy (EDS) analyses were performed on a HITACHI SU5000 field-emission scanning electron microscope operated at 20 kV. Optical microscopy was performed on an Olympus DSX1000 digital stereomicroscope coupled with a 40 × objective lens. Transmission electron microscopy (TEM) and high angular annular dark field scanning TEM (HAADF-STEM) images were captured on a JEOL JEM-2800 microscope equipped with an EDS detector. X-ray diffraction (XRD) measurements were recorded on a PANalytical X'pert diffractometer operating at 40 kV using Cu K$_\alpha$ radiation (λ = 0.154178 nm). X-ray photoelectron spectroscopy (XPS) was performed using a Thermo Fischer ESCALAB 250Xi spectrophotometer with the X-ray source of monochromatic aluminum. In situ Raman spectra were collected using an inVia-Reflex confocal Raman microscope in a customized in situ electrochemical flow cell. The excitation wavelength was 532 nm. Each spectrum was an average of three measurements acquired over 30 s. Ex-situ Raman spectra were collected under ambient air conditions. The porosities were determined from nitrogen isothermal adsorption-desorption experiments at 77 K using a Micromeritics ASAP 2020 apparatus. The specific area was obtained based on Brunauer−Emmett−Teller (BET) model. Thermogravimetric analysis (TGA) was carried out with a STA449F3 Jupiter thermal analysis system. Measurements were conducted by heating from room temperature to 1000 °C at a heating rate of 10 °C min^{-1} under air atmosphere. The oxygen release behavior and contact angles (CA) were recorded using Attension Theta. Gas-bubble adhesive force tests were performed using Kruss K100 (Germany).

2.5. Electrochemical measurements

The electrochemical measurements were performed at room temperature using a three-electrode configuration on an electrochemical workstation (Gamry Reference600) after *iR* correction. A graphite rod and Hg/HgO (1 M KOH solution) were used as the counter and the reference electrode, respectively. Measurements were performed in aqueous KOH solution. For powder samples, catalysts ink was prepared by ultrasonic mixing of 5 mg catalysts powder, 0.2 mL water, 0.8 mL ethanol and 30 μL 5 % Nafion solution. 4.5 μL of the above ink was dropped onto a glassy carbon (GCE, 3 mm diameter) electrode and dried in air. The working electrode was activated in the electrolyte by cycling at a scan rate of 50 mV s^{-1} for 30 cycles (except pseudocapacitive behavior). Current densities were normalized to the geometrical area. The measured potentials were corrected to the reversible hydrogen electrode (RHE): E(RHE) = E(Hg/HgO) + 0.098 + 0.0591 × pH. The overpotential (η) was calculated according to the equation: η = E(RHE) − 1.23 V. Linear sweep voltammetry (LSV) and cyclic voltammetry (CV) measurements were carried out at a scan rate of 5 mV s^{-1}. The

corresponding Tafel slope was calculated according to the LSV plot by the following equation, $\eta = b \times \log J + a$, where J is the current density, and b is the Tafel slope. Electrochemical impedance spectroscopy (EIS) was executed in a frequency range of 10^5 Hz to 0.1 Hz. Electrochemical active surface area (ECSA) was determined using an electrochemical double-layer capacitance (C_{dl}) method. After scanning CV curves in a non-Faradaic region in 1 M KOH electrolyte at different scan rates (10, 20, 30, 40, 50, and 60 mV s^{-1}), C_{dl} values were measured from slopes by fitting current densities between anodic and cathodic sweeps at a fixed potential against the scan rate.

3. Results and discussion

3.1. Structural characterizations of FeCoNiO$_x$/C/NF

FeCoNiO$_x$/C/NF electrocatalysts with 3D network structures are fabricated using a facile impregnation-foaming-calcination method. As shown in Fig. 1, NF was impregnated in an aqueous gel containing chitosan and metal salts. After foaming and drying in an oven, FeCoNiO$_x$/C/NF electrocatalysts were obtained by calcinating. The color of the NF substrate changed from metallic gray and brown to black during the process (Fig. S1a). It should be noted that this method is not limited by sample size and beneficial to large-scale production of electrode materials for EWS (Fig. S2).

The optical images show that FeCoNiO$_x$/C/NF electrocatalysts exhibit 3D porous network structures (Fig. 2a and S1). The 3D structures are also confirmed in scanning electron microscopy (SEM) image (Fig. 2b). Energy dispersive X-ray spectroscopy (EDS) mapping reveals uniform distribution of Fe, Co, Ni, C, N and O elements throughout the 3D network (Fig. 2c-i). To investigate the structure at nanoscale, FeCoNiO$_x$/C is peeled from FeCoNiO$_x$/C/NF. Fig. 2j shows high-angle annular dark field-scanning transmission electron microscopy (HAADF-STEM) image. The corresponding profile analysis of elements is illustrated in the inset of this image. These results suggest that elements of Fe, Co, Ni, C, N, and O are uniformly dispersed at nanoscale. The dispersion of elements is verified using STEM-EDS mapping (Fig. 2k-p and S3). The atomic ratio of Fe/Co/Ni is 1.84:4.2:1.4 in FeCoNiO$_x$/C (Fig. S3c). High-resolution TEM (HR-TEM) image of FeCoNiO$_x$/C displays an interplanar spacing of 0.245 nm, corresponding to the (311) planes of spinel NiCo$_2$O$_4$ (Fig. 2q). Crystals are surrounded by an amorphous carbon layer. Particle size distribution is illustrated in

Fig. S4. The mean size is determined to be 9.35 nm. The contents of FeCoNiO$_x$ spinel are 91.8 wt % in FeNiCoO$_x$/C according to the thermogravimetric analysis (TGA), as shown in Fig. S5a. N$_2$ adsorption−desorption isotherms of FeCoNiO$_x$/C show a type H2 hysteresis with a Brunauer−Emmett−Teller (BET) surface area of 69.8 m^2 g^{-1} (Fig. S5b), in agreement with many inorganic oxides incorporated in a complex network containing interconnected narrow pores [35]. Barrette–Joynere–Halenda (BJH) results (Fig. S5c) indicate that pore sizes are mainly distributed in the range from 2 to 15 nm. The large surface area and porous structure of FeCoNiO$_x$/C is expected to be favorable for mass transportation and exposing active sites for OER [36]. In addition, we prepared CoO$_x$/C/NF, FeCoO$_x$/C/NF, and NiCoO$_x$/C/NF as OER electrocatalysts in control experiments. These samples show structures similar to FeCoNiO$_x$/C/NF.

The crystallinity and phase purity of samples are verified using X-ray diffraction (XRD). According to Fig. 3a and S6 (FeNiCo-gels precursors calcined at different temperatures), the peaks located at 19.0°, 31.1°, 36.6°, 44.6°, 55.3°, 59.0°, and 64.7° are indexed to (111), (220), (311), (400), (422), (511), and (440) planes of the cubic spinel-type NiCo$_2$O$_4$ (JCPDS No. 20-0781) for FeCoNiO$_x$/C, FeCoO$_x$/C, and NiCoO$_x$/C [37]. The diffraction peaks at 19.0°, 31.3°, 36.9°, 44.8°, 55.7°, 59.4°, and 65.3° for CoO$_x$ can be indexed to the (111), (220), (311), (400), (422), (511), and (440) planes of cubic spinel Co$_3$O$_4$ (JCPDS card No. 74–4657, space group: Fd$\bar{3}$m) [38]. There is a negative shift (0.19°) in peaks for multi-metallic spinels compared to Co$_3$O$_4$, which could be due to the lattice expand induced by element doping [38–40].

Raman spectroscopy is used to illustrate cation distributions in spinel phases in terms of vibrational dynamics. In Fig. 3b, the peaks at 531 and 457 cm^{-1} appear in all samples, which can be ascribed to F$_{2g}^{(2)}$ and E$_g$ modes, respectively [9,41,42]. As for CoO$_x$/C, the peaks located at 187 and 651 cm^{-1} are ascribed to F$_{2g}^{(1)}$ (CoO$_4$) and A$_{1g}$ (CoO$_6$) modes of Co$_3$O$_4$, indicating that CoO$_x$ crystals have normal spinel structures with one tetrahedrally coordinated Co^{2+} (CoO$_4$) and two octahedrally coordinated Co^{3+} (CoO$_6$) sites [38]. While the peak related to the F$_{2g}^{(1)}$ mode keeps unchanged, the one related to A$_{1g}$ shifts to high wave number of 667 cm^{-1} in multi-metallic samples, suggesting that Ni or Fe ions are introduced in CoO$_6$ sites to form inverse spinel structures. When Fe and Ni elements are co-doped, the peak related to the F$_{2g}^{(1)}$ mode shifts to low wave number of 181 cm^{-1}, and it becomes weak and broad in FeCoNiO$_x$/C, revealing that CoO$_4$ sites are occupied by Fe and Ni atoms in accompany with destruction of symmetry [38,43].
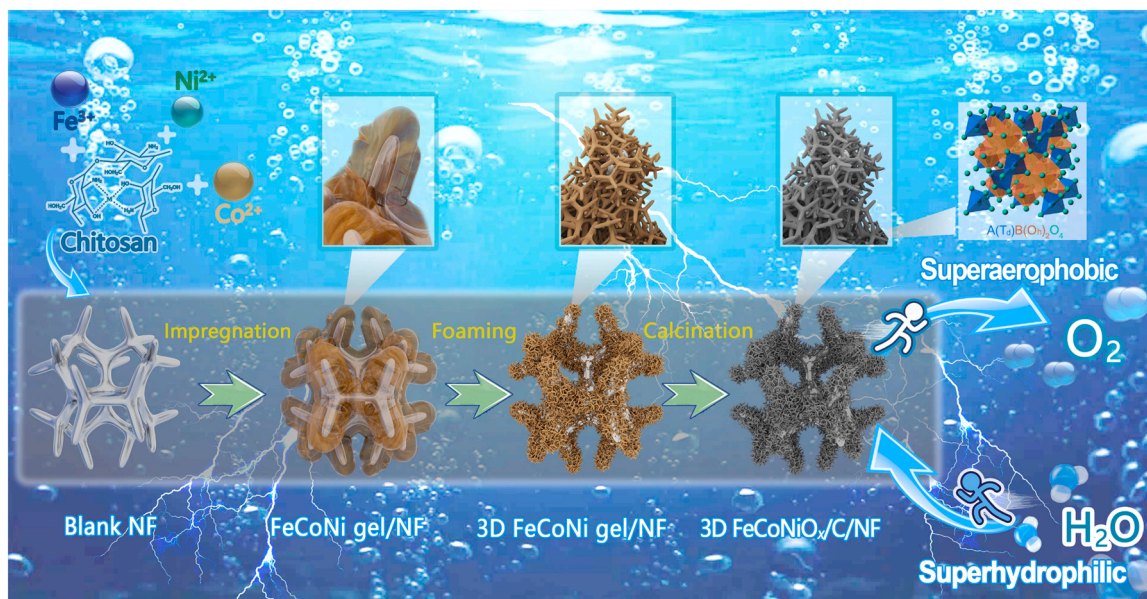

Fig. 1. Schematic illustration for constructing FeCoNiO$_x$/C/NF electrocatalysts with 3D network structures using an impregnation-foaming-calcination method.
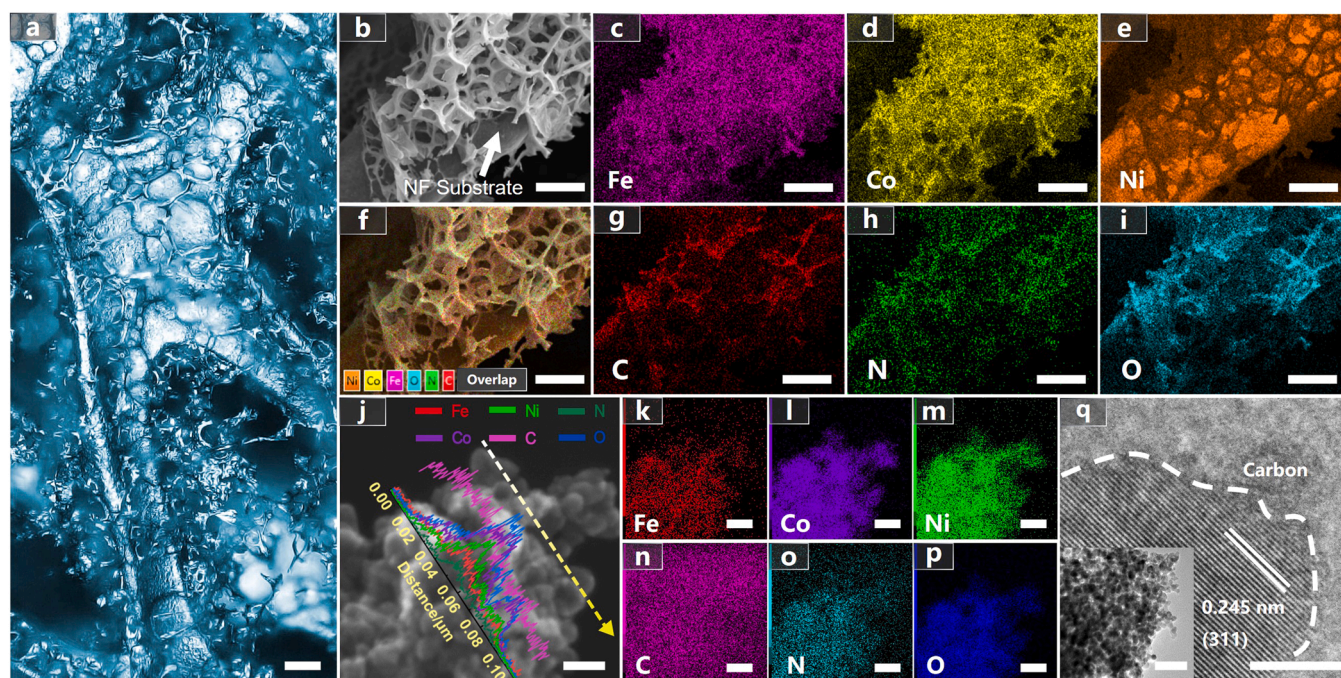
Fig. 2. Morphology characterizations. a) Optical microscopic photograph of FeCoNiO$_x$/C/NF electrocatalysts. b-i) SEM images and corresponding elemental mapping of FeCoNiO$_x$/C/NF. Scale bars: a-i 25 μm. j-p) HAADF-STEM images and corresponding line scans and elemental mapping peeled FeCoNiO$_x$/C from FeCoNiO$_x$/C/NF. Scale bars: j-p 20 nm. q) HRTEM image of FeCoNiO$_x$/C (Inset is a low-magnification TEM image). Scale bars: q 5 nm (50 nm in inset).
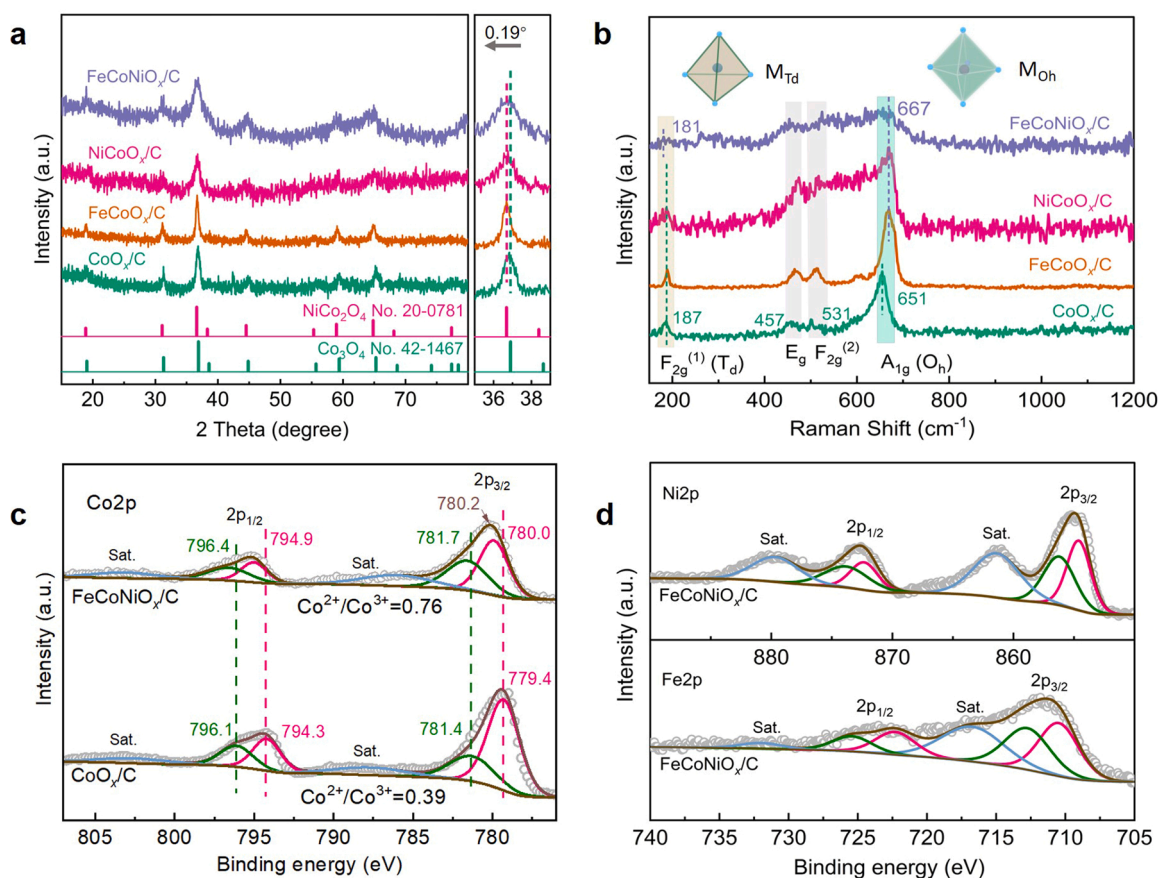

Fig. 3. a) XRD patterns and b) Raman spectra of CoO$_x$/C, FeCoO$_x$/C, NiCoO$_x$/C and FeNiCoO$_x$/C electrocatalysts. High-resolution XPS spectra of c) Co 2p for CoO$_x$/C and FeNiCoO$_x$/C, d) Ni 2p and Fe 2p for FeNiCoO$_x$/C electrocatalysts.

X-ray photoelectron spectroscopy (XPS) was performed to study the chemical composition and the valence states of FeNiCoO$_x$/C. The XPS survey scan and high-resolution spectra for C, N, and O are also given in Figs. S7 and S8, respectively, confirming the successful synthesis of metal oxides [44,45]. Fig. 3c shows Co2p XPS high-resolution spectra are indexed to Co state of Co2p$_{3/2}$ and Co2p$_{1/2}$ orbitals, illustrating the co-existence of Co^{3+} (779.4 and 794.3 eV) and Co^{2+} (781.4 and 796.1 eV) oxidation states for monometallic Co based catalyst [46–48]. Compared with pristine Co based spinel catalyst, the sample of FeCoNiO$_x$/C has the higher binding energy for Co2p, suggesting the charge transfer from Fe/Ni to Co. Fig. 3d displays Ni2p and Fe2p XPS spectra of as-obtained FeNiCoO$_x$/C catalyst. There are all two pairs of spin-orbit doublets originated from 2p$_{3/2}$ and 2p$_{1/2}$ with two shakeup satellites. The Ni2p spectra present two peaks in each spin-orbit doublet, characteristic of Ni^{2+} and Ni^{3+} in spinel respectively [49,50]. Fe2p peaks related to Fe2p3/2 (710.5 and 712.9 eV) and Fe2p1/2 (722.6 and 725.5 eV) indicate the existence of Fe^{3+}, revealing Fe^{3+} equally distributed between Oh and Td sites of the O^{2-} fcc cell [45].

3.2. Superhydrophilic/Superaerophobic Catalyst properties

The features of the solid-liquid (electrode-electrolyte) and solid-air (electrode-oxygen) contact interface serve as an important role in OER catalysis process [51]. The contact angles were measured to evaluate their superhydrophilic/superaerophobic properties. As shown in Fig. 4a–d, blank NF exhibits a strong hydrophobicity with a solid-liquid contact angle of 110°. In contrast, the water droplet dispersed immediately as it was loaded on FeCoNiO$_x$/C/NF (Fig. 4f–i), demonstrating superhydrophilic properties, which could facilitate access of electrolyte to active sites during OER. The animated process is illustrated in Supporting Information (video 1 and 2). To evaluate the superaerophobic properties, the solid-air contact angle was measured in aqueous solution. FeCoNiO$_x$/C/NF possesses larger solid-air contact angle (152°) than blank NF (133°) (Fig. 4i and j). The dynamic O$_2$ release behaviors were studied at a current density of 10 mA cm^{-2} during OER (Fig. 4k–n). The corresponding process is recorded in Supporting Information (video 3). Blank NF accumulates a large number of O$_2$ bubbles on the surface. In contrast, only a few tiny bubbles appear on FeCoNiO$_x$/C/NF during the reaction. The size distribution of O$_2$ bubbles is illustrated in Fig. S9. The average size of O$_2$ bubbles is 0.12 mm and 0.20 mm on surfaces of
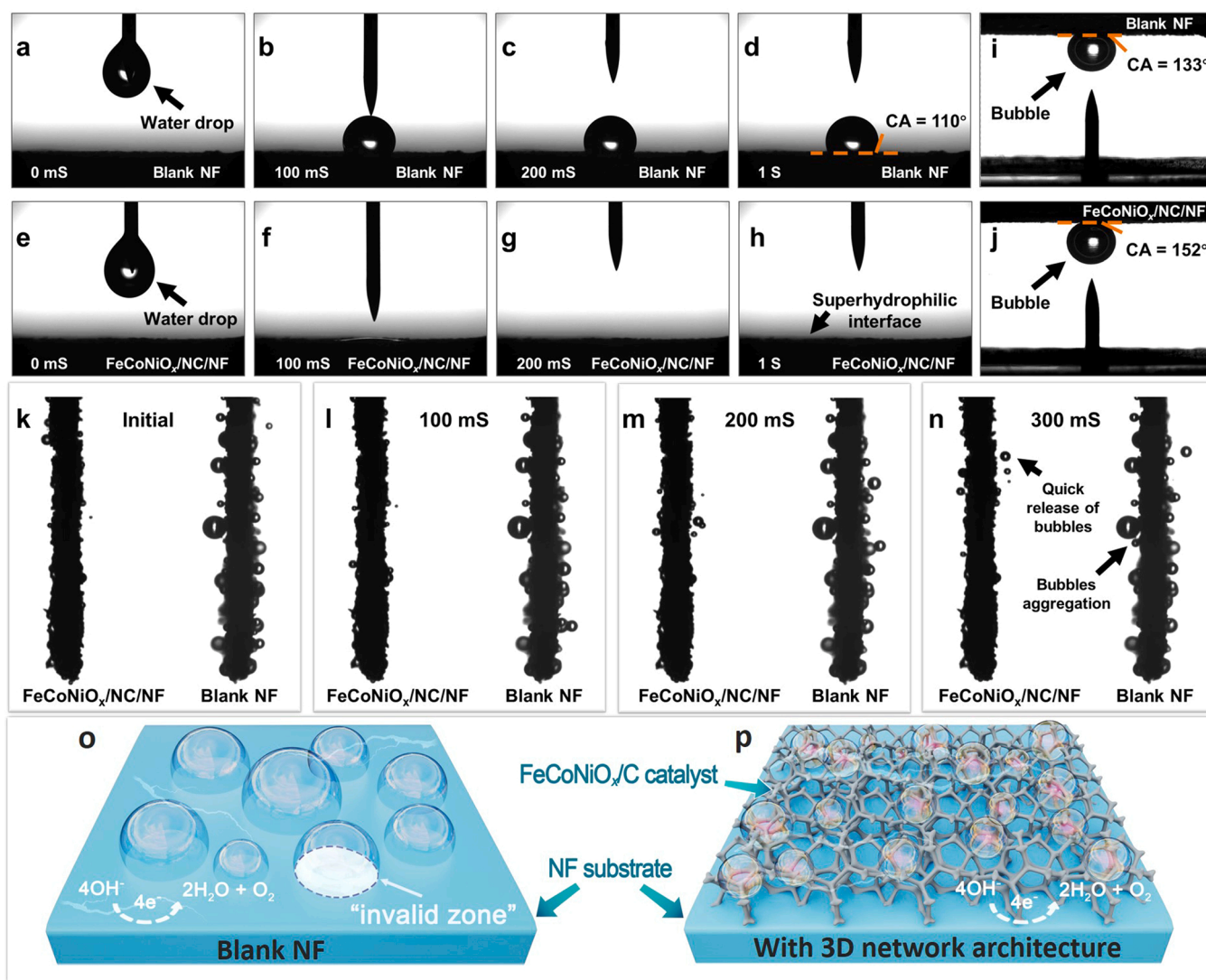

Fig. 4. Superhydrophilicity/superaerophobicity properties of FeCoNiO$_x$/C/NF. a-d) Solid-liquid contact angle of blank NF. e-h) Solid-liquid contact angle of FeCoNiO$_x$/C/NF electrode. i-j) Solid-air contact angles of blank NF and as-synthesized FeCoNiO$_x$/C/NF electrode in water, respectively. k-n) In situ observations of oxygen release behavior on the electrode surfaces at the current density of 10 mA cm^{-2} in 1 M KOH solution. o-p) Schematic display that the superaerophobic property of 3D network architecture for boosting the release of O$_2$ bubbles during OER.

FeCoNiO$_x$/C/NF and blank NF, respectively. Moreover, O$_2$ bubbles show narrow size distribution on the surface of FeCoNiO$_x$/C/NF relative to blank NF (Fig. S9). The state of O$_2$ bubbles on electrode is vividly illustrated in Fig. 4o and p. In order to illustrate the releasing behavior of in-situ generated O$_2$ bubbles, we performed the adhesive force test for air bubbles on various electrodes. In Figs. S10a and b, Stage 1, 2 and 3 refer to the surface of electrodes approaching, moving away but still being contact with, and departing from the air bubble, respectively (Fig. S10). Apparent deformation of bubbles is observed in Inset 2′ of Fig. S10a, indicating strong adhesion (49.2 μN) of bubbles to blank NF. In contrast, FeCoNiO$_x$/C/NF displays negligible interaction with gas-bubble (Inset 2′ of Fig. S10b), suggesting that the in-situ generated O$_2$ bubbles can be released from the electrode easily and timely.

Supplementary material related to this article can be found online at doi:10.1016/j.apcatb.2023.122717.

The life-cycle of bubbles on OER electrodes includes stages of nucleation, growth, coalescence, and detachment (Fig. S10c) [52]. Since O$_2$ bubbles are prone to be pinned on blank NF due to strong adhesion, coalescence is dominant in competition with detachment, and an invalid zone is readily formed that is inaccessible to electrolytes (Fig. S10d), resulting in large IR drops and overpotentials for NF. In contrast, FeCoNiO$_x$/C/NF shows low contact region with bubbles due to the hierarchical surfaces with the discontinuous three-phase contact line [51,

53]. Moreover, the inter-connected channels on FeCoNiO$_x$/C/NF not only play the role of pathway for O$_2$ diffusion, but hinder coalescence sterically. As such, detachment is dominant on FeCoNiO$_x$/C/NF electrodes (Fig. S10e). In addition, electrolyte solutions can easily penetrate the porous surface by capillary force, promoting the detachment of O$_2$ bubbles [19,54]. Therefore, FeCoNiO$_x$/C/NF electrodes with 3D porous network structures can release the in-situ generated O$_2$ bubbles efficiently.

3.3. Electrocatalytic OER performance

The OER electrocatalytic performance was measured in 1.0 M KOH electrolyte. Fig. 5a displays the linear sweep voltammetry (LSV) at scan rate of 5 mV s^{-1}. Measurements were conducted from 1.7 to 0.9 V vs. RHE to avoid redox peaks. Fig. 5b shows Tafel plots based on LSV curves. The overpotentials at 10 mA cm^{-2} from LSV and Tafel slopes are illustrated in Fig. 5c: blank NF (292 mV, 71 mV dec^{-1}), monometallic FeO$_x$/C/NF (301 mV, 96 mV dec^{-1}), CoO$_x$/C/NF (264 mV, 53 mV dec^{-1}) and NiO$_x$/C/NF (359 mV, 100 mV dec^{-1}), bimetallic CoFeO$_x$/C/NF (286 mV, 69 mV dec^{-1}) CoNiO$_x$/C/NF (225 mV, 43 mV dec^{-1}) and NiFeO$_x$/C/NF (248 mV, 50 mV dec^{-1}), and trimetallic FeCoNiO$_x$/C/NF (221 mV, 21 mV dec^{-1}). As such, FeCoNiO$_x$/C/NF electrode shows both smallest values in overpotential and Tafel slope among these samples.
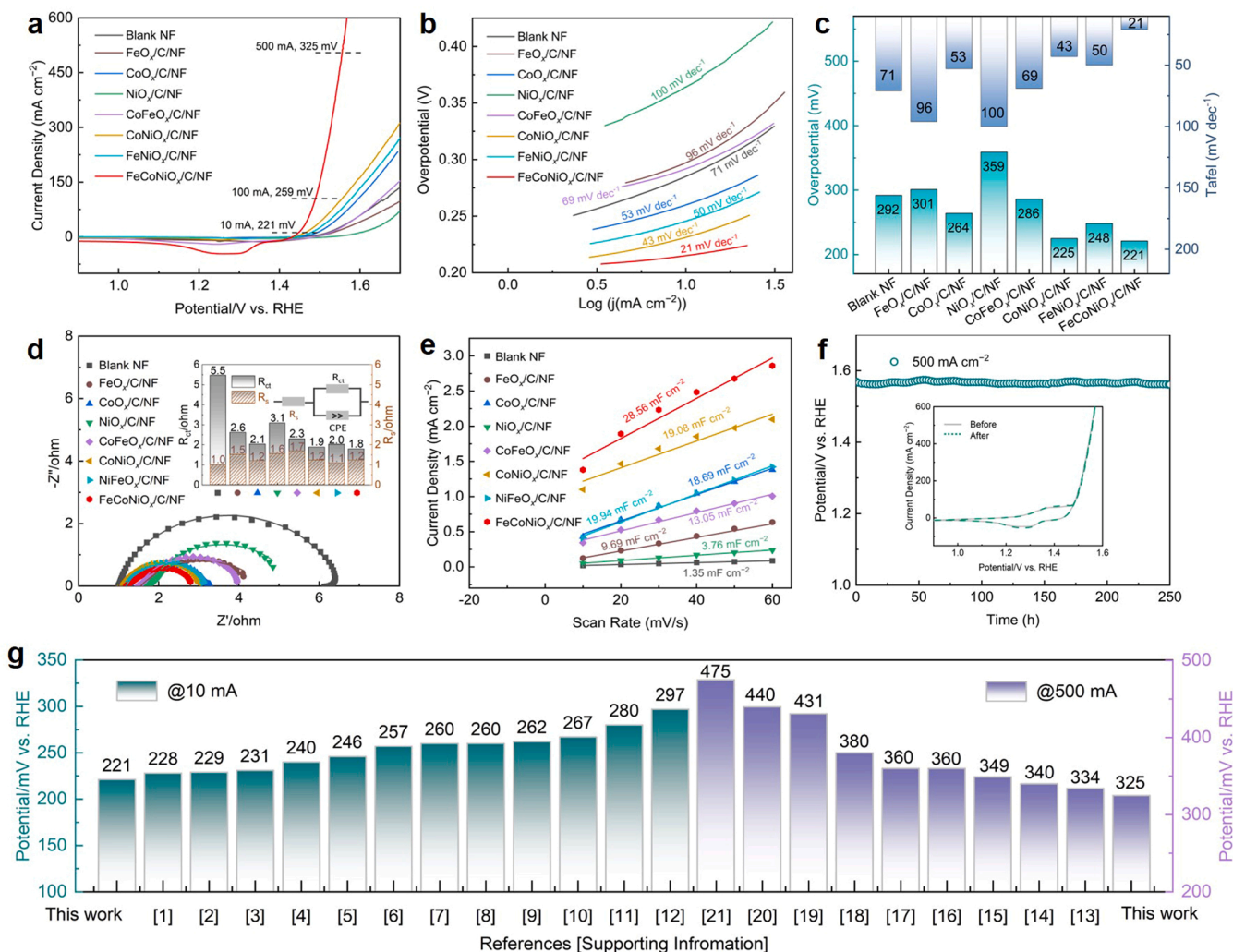

Fig. 5. Electrochemical performance in 1.0 M KOH. a) Polarization curves at scan rate of 5 mV s^{-1} and b) the corresponding Tafel plots. c) Comparison of the overpotentials obtained at 10 mA cm^{-2} and Tafel slopes. d) EIS Nyquist plots at 10 mA cm^{-2}. e) Plots of the double layer charging current against scan rates to calculate C_{dl}. f) Durability tests of 3D FeCoNiO$_x$/C/NF electrode materials (inset is the polarization curves before and after 250 h test). g) Comparison of the overpotential of OER at 10 and 500 mA cm^{-2} with other recently reported advanced catalysts in 1 M KOH electrolyte (the corresponding data are listed in Table S2).

The low Tafel slope of 21 mV dec^{-1} indicates a favorable kinetics pathway for FeCoNiO$_x$/C/NF [55,56]. In addition, FeCoNiO$_x$/C/NF electrode shows low overpotential at high current density of 100 mA cm^{-2} (259 mV) and 500 mA cm^{-2} (325 mV), respectively (Fig. 5a). Furthermore, we prepare FeCoNiO$_x$/C electrodes with different atomic ratio of Fe/Co/Ni by tuning the feed ratios of metal salts during chitosan gel formation. The sample with Fe/Co/Ni ratio of 1:2:1 shows the lowest overpotential (Fig. S11). As such, we speculate that the electrocatalytic performance of FeCoNiO$_x$/C/NF electrodes can be further improved by tuning the atomic ratio of metal ions, which will be investigated in the future work. All the results indicate that the trimetallic FeCoNiO$_x$/C/NF electrode has the best performance among these spinel samples. In Fig. S12, the overpotential of non-metal carbon/NF is slightly high relative to blank NF, suggesting carbon has negligible contribution to OER. Meanwhile, the catalytic performance of FeCoNiO$_x$/C/NF is superior to the commercial RuO$_2$ catalyst. Electrochemical impedance spectroscopy (EIS) was used to analyze charge transfer characteristics of samples (the corresponding fitting data are listed in Table S1). Nyquist curves show that FeCoNiO$_x$/C/NF electrode presents small charge transfer resistance (R_{ct} = 1.8 Ω) compared with other samples (Fig. 5d), which can be related to the enhanced intrinsic activities due to trimetallic synergistic effect [57–59]. The double-layer capacitance (C_{dl}) base on cyclic voltammograms was used to estimate electrochemical active surface areas (ECSA, Fig. S13). C_{dl} values were obtained by plotting the double layer charging current against scan rates (Fig. 5e). FeCoNiO$_x$/C/NF electrode has the largest C_{dl} value of 28.56 mF cm^{-2} among these samples, indicating the trimetallic spinel electrode exposes a great active surface area. Stability tests were measured using a chronopotentiometry (CP) method. First, we conducted the experiment at room temperature in 1 M KOH solution at 500 mA cm^{-2}. FeCoNiO$_x$/C/NF electrode shows an excellent stability without apparent decay in 250 h (Fig. 5f). Moreover, CV curves show negligible changes for this electrode before and after the stability test (inset in the Fig. 5f). Second, in pursuit of potential application under industry conditions, we conducted CP tests at a high temperature in 6 M KOH electrolyte at 1000 mA cm^{-2} [60]. Due to the temperature limit of Hg/HgO reference

electrode, the measurement was carried out at 50 °C. Fig. S14 shows that FeCoNiO$_x$/C/NF electrodes can maintain good stability with only a slight increase in overpotential (30 mV) after 25 h.

To shed light on the excellent OER performance in basic conditions, the structure of FeCoNiO$_x$/C/NF electrodes after the stability test were characterized using XRD, TEM, and XPS. Fig. S15 shows TEM images of FeCoNiO$_x$/C peeled from FeCoNiO$_x$/C/NF. In Fig. S15b, an interplanar spacing of 0.203 nm is ascribed to the (400) planes of spinel NiCo$_2$O$_4$. STEM-EDS mapping indicates the uniform distribution of Fe, Co, Ni, C, N, O, and K, where K comes from the electrolyte (Figs. S15d-j). XRD patterns verify that the sample can keep the spinel phase (Fig. S16a). However, the peak shifts from 780.2 to 779.6 eV, and the area ratio of Co^{2+}/Co^{3+} decreased from 0.76 to 0.68 in high resolution XPS spectra of Co after the 250 h stability test (Fig. S16), which might result from formation of CoOOH [61–63]. In contrast, no noticeable changes are observed in both Ni2p and Fe2p spectra. In Fig. S16h, the peak associated with metal oxides (529.2 eV) shifts to low binding energy compare with the sample before OER test (592.6 eV, Fig. S8f), which further verifies the formation of oxyhydroxide species (CoOOH) [64]. These results confirm that Co is the active site for OER in FeCoNiO$_x$/C/NF. Meanwhile, the unchanged superhydrophilic/superaerophobic properties demonstrated the structure stability of FeCoNiO$_x$/C/NF (Fig. S17).

Next, we investigate the performance of spinel electrocatalysts using NF free electrodes. In this experiment, FeCoNiO$_x$/C was scrapped from FeCoNiO$_x$/C/NF, and loaded on glassy carbon electrode (GCE) to avoid any interference caused by NF. In Fig. 6a, the shifts of CV curves are detected during cycling for all samples, suggesting that spinel catalysts might undergo an irreversible surface reconstruction into oxyhydroxides [39]. A pair of redox peaks are observed for CoO$_x$/C catalyst, and the anodic peak (1.45 V vs. RHE) and cathodic peak (1.42 V vs. RHE) can be assigned to Co(III)/Co(IV) redox couple in 1st cycle [65–67], yet these peaks are not shown for multi-metallic spinel catalysts, which could result from their overlap with multiple redox processes associated with Ni and Fe species. In the potential range from 1.58 to 1.60 V vs. RHE, only Fe-containing catalysts exhibit an increase in the current density at 1.6 V vs. RHE over cycling, in agreement with previous study suggesting
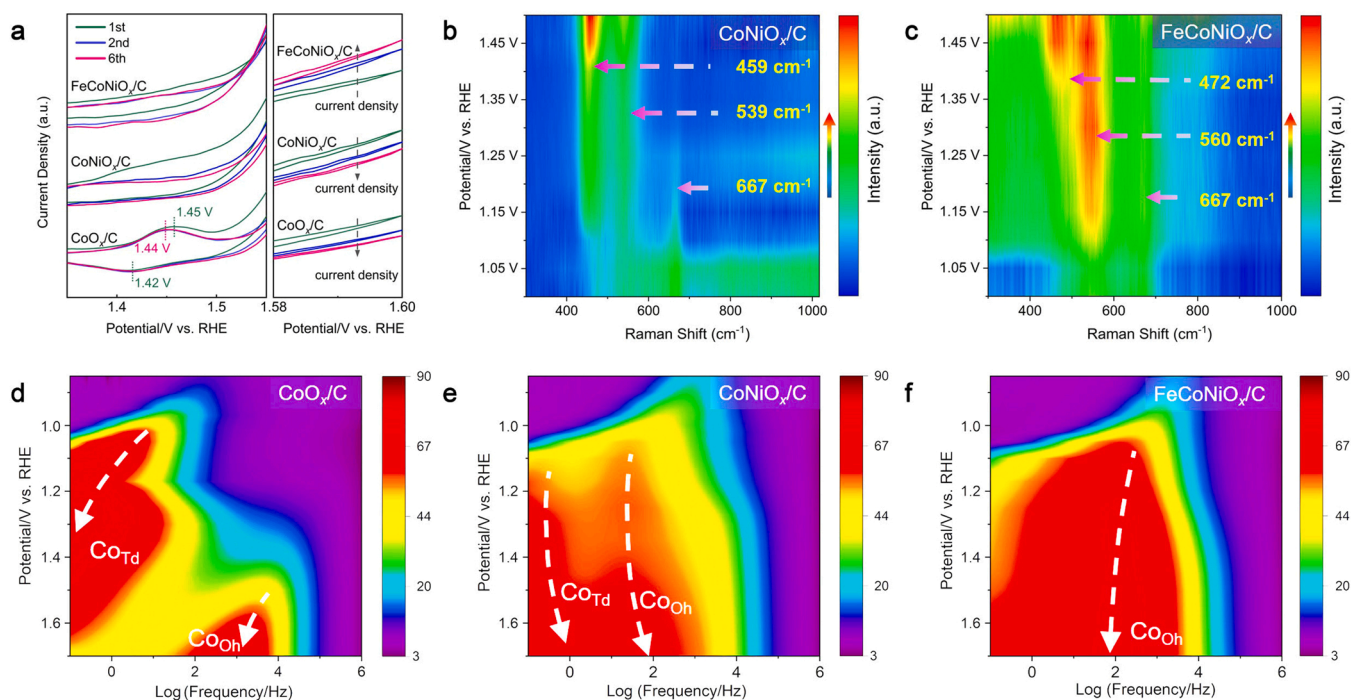

Fig. 6. In situ investigate the effect of Fe in structural transformation of catalysts. a) Pseudocapacitive behavior in the first, second and sixth cycles of CV cycling at a scan rate of 10 mV s^{-1}. b-c) In situ Raman spectra for CoNiO$_x$/C and FeCoNiO$_x$/C in the potential range from 1.0 to 1.5 V vs. RHE. d-f) 2D contour Bode plots for CoO$_x$/C, CoNiO$_x$/C and FeCoNiO$_x$/C, respectively.

that the catalytic activity of spinels can be increased by doping (Fig. 6a) [31]. To verify this hypothesis, we recorded in situ potential-dependent Raman spectra in 1 M KOH. According to Fig. 6b and c, the peak at 667 cm^{-1} is assigned to Co$_{Oh}$-O vibration mode for both NiCoO$_x$/C and FeNiCoO$_x$/C, which is less affected by applied potential. In contrast, peaks at 459 cm^{-1} (E$_g$) and 539 cm^{-1} (A$_{1\,g}$) associated with CoOOH (OER active species) increase with applied potential in NiCoO$_x$/C (Fig. 6b) [68–70]. These two peaks shift to high wave number of 472 cm^{-1} (E$_g$) and 560 cm^{-1} (A$_{1g}$) in FeNiCoO$_x$/C, which could be caused by lattice distortion due to Fe doping that leads to bond compression and charge redistribution [71,72]. In addition, the two peaks show strong intensity in FeNiCoO$_x$/C relative to NiCoO$_x$/C, indicating that Fe doping can facilitate the formation of CoOOH species.

To further investigate the effect of Fe doping on OER, in situ electrochemical impedance spectroscopy (EIS) measurements were carried out over a frequency range from 10^5 to 0.1 Hz under applied potentials from 0.9 to 1.65 V vs RHE [73]. Fig. 6d-f show 2D contour Bode plots CoO$_x$/C, CoNiO$_x$/C and FeCoNiO$_x$/C, where peak loci of phase angles (Fig. S18) are highlighted with dashed arrows for recognizing OER active Co coordination geometries [66]. CoO$_x$/C exhibits two distinctive loci at low frequency region (10^{-1}–10 Hz) and high frequency region (10^2 – 10^4 Hz), which are assigned to Co$_{Td}$ and Co$_{Oh}$ sites, respectively (Fig. 6d) [74–76]. CoNiO$_x$/C also has two loci, similar to those in CoO$_x$/C, confirming the co-existence of Co$_{Oh}$ and Co$_{Td}$ in the catalyst (Fig. 6e). However, a single locus presents at frequency region of 1.8–2.2 × 10^3 Hz in FeCoNiO$_x$/C, suggesting that catalytic reactions are primarily initiated at high active Co$_{Oh}$ sites (Fig. 6f) [75–79]. The position of phase angle peak can be influenced by the charger transfer activity. Peaks at low and high frequency region are associated with charger transfer conductivity at the electrode-electrolyte interface and electronic conductivity of catalysts, respectively [73,80–82].

4. Conclusions

FeCoNi/C/NF electrocatalyst with 3D porous network architecture was synthesized by an impregnation-foaming-calcination method. This method is affordable, simple, low cost, and easy to large-scale preparation. The FeCoNi/C/NF electrodes demonstrate superhydrophilic/superaerophobic properties, which facilitate O$_2$ release. Our result shows that Fe doping can lead to enhanced intrinsic activities. On one hand, small charge transfer resistance is observed which could be due to trimetallic synergistic effect. On the other hand, in situ EIS result suggests that Fe doping can promote the reaction initiated at high active Co$_{Oh}$ sites. As such, FeCoNi/C/NF electrodes show small overpotentials of 221 mV at 10 mA cm^{-2} and 325 mV at high current density of 500 mA cm^{-2} in 1 M KOH. Overpotential decay is not observed for 250 h at 500 mA cm^{-2}, demonstrating their good stability. Under industry conditions (6 M KOH at 50 °C), FeCoNiO$_x$/C/NF electrodes exhibit a low overpotential of 295 mV at 1000 mA cm^{-2}, and only a slight increase in overpotential (30 mV) is observed after 25 h.

CRediT authorship contribution statement

Liang Ma: Conceptualization, Writing – original draft. **Zengyan Wei:** Methodology, Writing – review & editing. **Chen Zhao:** Visualization. **Xiangyu Meng:** Software. **Honglei Zhang:** Software. **Meixiu Song:** Investigation. **Yaming Wang:** Validation. **Baoqiang Li:** Validation. **Xiaoxiao Huang:** Resources. **Chengyan Xu:** Resources, Methodology. **Ming Feng:** Resources, Methodology. **Peigang He:** Conceptualization, Data curation. **Dechang Jia:** Resources, Conceptualization. **Yu Zhou:** Resources, Conceptualization. **Xiaoming Duan:** Conceptualization, Validation, Supervision.

Declaration of Competing Interest

The authors declare that they have no known competing financial interests or personal relationships that could have appeared to influence the work reported in this paper.

Data Availability

Data will be made available on request.

Appendix A. Supporting information

Supplementary data associated with this article can be found in the online version at doi:10.1016/j.apcatb.2023.122717.

References

[1] A. Abdelhafiz, B. Wang, A.R. Harutyunyan, J. Li, Carbothermal shock synthesis of high entropy oxide catalysts: dynamic structural and chemical reconstruction boosting the catalytic activity and stability toward oxygen evolution reaction, Adv. Energy Mater. 12 (2022) 2200742, https://doi.org/10.1002/aenm.202200742.

[2] Y. Kim, D. Kim, J. Lee, L.Y.S. Lee, D.K.P. Ng, Tuning the electrochemical properties of polymeric cobalt phthalocyanines for efficient water splitting, Adv. Funct. Mater. 31 (2021) 2103290, https://doi.org/10.1002/adfm.202103290.

[3] X. Gao, H. Zhang, Q. Li, X. Yu, Z. Hong, X. Zhang, C. Liang, Z. Lin, Hierarchical NiCo$_2$O$_4$ hollow microcuboids as bifunctional electrocatalysts for overall water-splitting, Angew. Chem. Int. Ed. 55 (2016) 6290–6294, https://doi.org/10.1002/anie.201600525.

[4] F. Hu, D. Yu, M. Ye, H. Wang, Y. Hao, L. Wang, L. Li, X. Han, S. Peng, Lattice-matching formed mesoporous transition metal oxide heterostructures advance water splitting by active Fe–O–Cu bridges, Adv. Energy Mater. 12 (2022) 2200067, https://doi.org/10.1002/aenm.202200067.

[5] S.M. Thalluri, L. Bai, C. Lv, Z. Huang, X. Hu, L. Liu, Strategies for semiconductor/electrocatalyst coupling toward solar-driven water splitting, Adv. Sci. 7 (2020) 1902102, https://doi.org/10.1002/advs.201902102.

[6] N. Kumar, K. Naveen, M. Kumar, T.C. Nagaiah, R. Sakla, A. Ghosh, V. Siruguri, S. Sadhukhan, S. Kanungo, A.K. Paul, Multifunctionality exploration of Ca$_2$FeRuO$_6$: an efficient trifunctional electrocatalyst toward OER/ORR/HER and photocatalyst for water splitting, ACS Appl. Energy Mater. 4 (2021) 1323–1334, https://doi.org/10.1021/acsaem.0c02579.

[7] F.H. Wang, B.B. Dong, J.W. Wang, N.W. Ke, C.T. Tan, A.D. Huang, Y.T. Wu, L. Y. Hao, L.J. Yin, X. Xu, Y.X. Xian, S. Agathopoulos, Self-supported porous heterostructure WC/WO$_{3-x}$ ceramic electrode for hydrogen evolution reaction in acidic and alkaline media, J. Adv. Ceram. 11 (2022) 1208–1221, https://doi.org/10.1007/s40145-022-0604-4.

[8] Y. Gorlin, T.F. Jaramillo, A bifunctional nonprecious metal catalyst for oxygen reduction and water oxidation, J. Am. Chem. Soc. 132 (2010) 13612–13614, https://doi.org/10.1021/ja104587v.

[9] Y. Huang, S.L. Zhang, X.F. Lu, Z.-P. Wu, D. Luan, X.W.D. Lou, Trimetallic spinel NiCo$_{2-x}$Fe$_x$O$_4$ nanoboxes for highly efficient electrocatalytic oxygen evolution, Angew. Chem. Int. Ed. 60 (2021) 11841–11846, https://doi.org/10.1002/anie.202103058.

[10] S. Fan, J. Zhang, Q. Wu, S. Huang, J. Zheng, D. Kong, S. Chen, Y. Wang, L.K. Ang, Y. Shi, H.Y. Yang, Morphological and electronic dual regulation of cobalt-nickel bimetal phosphide heterostructures inducing high water-splitting performance, J. Phys. Chem. Lett. 11 (2020) 3911–3919, https://doi.org/10.1021/acs.jpclett.0c00851.

[11] H. Xu, J.-X. Feng, Y.-X. Tong, G.-R. Li, Cu$_2$O–Cu hybrid foams as high-performance electrocatalysts for oxygen evolution reaction in alkaline media, ACS Catal. 7 (2017) 986–991, https://doi.org/10.1021/acscatal.6b02911.

[12] G. Liu, M. Wang, Y. Wu, N. Li, F. Zhao, Q. Zhao, J. Li, 3D porous network heterostructure NiCe@NiFe electrocatalyst for efficient oxygen evolution reaction at large current densities, Appl. Catal. B Environ. 260 (2020) 118199, https://doi.org/10.1016/j.apcatb.2019.118199.

[13] Y.J. Son, K. Kawashima, B.R. Wygant, C.H. Lam, J.N. Burrow, H. Celio, A. Dolocan, J.G. Ekerdt, C.B. Mullins, Anodized nickel foam for oxygen evolution reaction in Fe-free and unpurified alkaline electrolytes at high current densities, ACS Nano 15 (2021) 3468–3480, https://doi.org/10.1021/acsnano.0c10788.

[14] H. Sun, C. Tian, G. Fan, J. Qi, Z. Liu, Z. Yan, F. Cheng, J. Chen, C.-P. Li, M. Du, Boosting activity on Co$_4$N porous nanosheet by coupling CeO$_2$ for efficient electrochemical overall water splitting at high current densities, Adv. Funct. Mater. 30 (2020) 1910596, https://doi.org/10.1002/adfm.201910596.

[15] M. Hao, V. Charbonneau, N.N. Fomena, J. Gaudet, D.R. Bruce, S. Garbarino, D. A. Harrington, D. Guay, Hydrogen bubble templating of fractal Ni catalysts for water oxidation in alkaline media, ACS Appl. Energy Mater. 2 (2019) 5734–5743, https://doi.org/10.1021/acsaem.9b00860.

[16] M. Bae, Y. Kang, D.W. Lee, D. Jeon, J. Ryu, Superaerophobic polyethyleneimine hydrogels for improving electrochemical hydrogen production by promoting bubble detachment, Adv. Energy Mater. 12 (2022) 2201452, https://doi.org/ 10.1002/aenm.202201452.

[17] X. Yu, Z.-Y. Yu, X.-L. Zhang, Y.-R. Zheng, Y. Duan, Q. Gao, R. Wu, B. Sun, M.-R. Gao, G. Wang, S.-H. Yu, "Superaerophobic" nickel phosphide nanoarray catalyst for efficient hydrogen evolution at ultrahigh current densities, J. Am. Chem. Soc. 141 (2019) 7537–7543, https://doi.org/10.1021/jacs.9b02527.

[18] Q. Hu, Z. Wang, X. Huang, Y. Qin, H. Yang, X. Ren, Q. Zhang, J. Liu, M. Shao, C. He, Integrating well-controlled core-shell structures into "superaerophobic" electrodes for water oxidation at large current densities, Appl. Catal. B Environ. 286 (2021), 119920, https://doi.org/10.1016/j.apcatb.2021.119920.

[19] R. Andaveh, G. Barati Darband, M. Maleki, A. Sabour Rouhaghdam, Superaerophobic/superhydrophilic surfaces as advanced electrocatalysts for the hydrogen evolution reaction: a comprehensive review, J. Mater. Chem. A 10 (2022) 5147–5173, https://doi.org/10.1039/D1TA10519A.

[20] Y.J. Kim, A. Lim, J.M. Kim, D. Lim, K.H. Chae, E.N. Cho, H.J. Han, K.U. Jeon, M. Kim, G.H. Lee, G.R. Lee, H.S. Ahn, H.S. Park, H. Kim, J.Y. Kim, Y.S. Jung, Highly efficient oxygen evolution reaction via facile bubble transport realized by three-dimensionally stack-printed catalysts, Nat. Commun. 11 (2020) 4921, https://doi.org/10.1038/s41467-020-18686-0.

[21] Y. Du, H. Tang, D. Zhang, H. Liu, Y. Chen, Z. Zhu, W. Yang, Z. Li, Y. Tang, C. Liu, Boosting electrocatalytic oxygen evolution: superhydrophilic/superaerophobic hierarchical nanoneedle/microflower arrays of $Ce_xCo_{3−x}O_4$ with oxygen vacancies, ACS Appl. Mater. Interfaces 13 (2021) 42843–42851, https://doi.org/10.1021/ acsami.1c11662.

[22] J. He, B. Hu, Y. Zhao, Superaerophobic electrode with metal@metal-oxide powder catalyst for oxygen evolution reaction, Adv. Funct. Mater. 26 (2016) 5998–6004, https://doi.org/10.1002/adfm.201602116.

[23] J. Yuan, X. Cheng, H. Wang, C. Lei, S. Pardiwala, B. Yang, Z. Li, Q. Zhang, L. Lei, S. Wang, Y. Hou, A superaerophobic bimetallic selenides heterostructure for efficient industrial-level oxygen evolution at ultra-high current densities, Nano-Micro Lett. 12 (2020) 104, https://doi.org/10.1007/s40820-020-00442-0.

[24] S. Cao, H. Huang, K. Shi, L. Wei, N. You, X. Fan, Z. Yang, W. Zhang, Engineering superhydrophilic/superaerophobic hierarchical structures of Co-CH@NiFe-LDH/ NF to boost the oxygen evolution reaction, Chem. Eng. J. 422 (2021) 130123, https://doi.org/10.1016/j.cej.2021.130123.

[25] J. Kibsgaard, I. Chorkendorff, Considerations for the scaling-up of water splitting catalysts, Nat. Energy 4 (2019) 430–433, https://doi.org/10.1038/s41560-019-0407-1.

[26] K. Zhu, X. Zhu, W. Yang, Application of in situ techniques for the characterization of nife-based oxygen evolution reaction (OER) electrocatalysts, Angew. Chem. Int. Ed. 58 (2019) 1252–1265, https://doi.org/10.1002/anie.201802923.

[27] A. Grimaud, A. Demortière, M. Saubanère, W. Dachraoui, M. Duchamp, M.-L. Doublet, J.-M. Tarascon, Activation of surface oxygen sites on an iridium-based model catalyst for the oxygen evolution reaction, Nat. Energy 2 (2017), https:// doi.org/10.1038/nenergy.2016.189.

[28] Q. Zhao, Z. Yan, C. Chen, J. Chen, Spinels: controlled preparation, oxygen reduction/evolution reaction application, and beyond, Chem. Rev. 117 (2017) 10121–10211, https://doi.org/10.1021/acs.chemrev.7b00051.

[29] Y. Peng, C. Huang, J. Huang, M. Feng, X. Qiu, X. Yue, S. Huang, Filling octahedral interstices by building geometrical defects to construct active sites for boosting the oxygen evolution reaction on $NiFe_2O_4$, Adv. Funct. Mater. 32 (2022) 2201011, https://doi.org/10.1002/adfm.202201011.

[30] J. Li, D. Chu, H. Dong, D.R. Baker, R. Jiang, Boosted oxygen evolution reactivity by igniting double exchange interaction in spinel oxides, J. Am. Chem. Soc. 142 (2020) 50–54, https://doi.org/10.1021/jacs.9b10882.

[31] S. Anantharaj, S. Kundu, S. Noda, "The Fe Effect": a review unveiling the critical roles of Fe in enhancing OER activity of Ni and Co based catalysts, Nano Energy 80 (2021), 105514, https://doi.org/10.1016/j.nanoen.2020.105514.

[32] J. Su, Y. Yang, G. Xia, J. Chen, P. Jiang, Q. Chen, Ruthenium-cobalt nanoalloys encapsulated in nitrogen-doped graphene as active electrocatalysts for producing hydrogen in alkaline media, Nat. Commun. 8 (2017) 14969, https://doi.org/ 10.1038/ncomms14969.

[33] Y. Zhang, B. Ouyang, J. Xu, S. Chen, R.S. Rawat, H.J. Fan, 3D porous hierarchical nickel-molybdenum nitrides synthesized by RF plasma as highly active and stable hydrogen-evolution-reaction electrocatalysts, Adv. Energy Mater. 6 (2016) 1600221, https://doi.org/10.1002/aenm.201600221.

[34] L. Zhang, C.-W. Hsu, X.-F. Chuah, S.-Y. Lu, Mixed $NiO/NiCo_2O_4$ /on of a 3D Porous Nickel Network as /actions, ACS Appl. Mater. Interfaces 10 (2018) 417–426, https://doi.org/10.1021/acsami.7b13127.

[35] R. Bardestani, G.S. Patience, S. Kaliaguine, Experimental methods in chemical engineering: specific surface area and pore size distribution measurements—BET, BJH, and DFT, Can. J. Chem. Eng. 97 (2019) 2781–2791, https://doi.org/10.1002/ cjce.23632.

[36] C. Zhou, X. Han, F. Zhu, X. Zhang, Y. Lu, J. Lang, X. Cao, H. Gu, Facile synthesis of the encapsulation of Co-based multimetallic alloys/oxide nanoparticles nirtogen-doped carbon nanotubes as electrocatalysts for the HER/OER, Int. J. Hydrogen Energy 47 (2022) 27775–27786, https://doi.org/10.1016/j.ijhydene.2022.06.104.

[37] A. Singh, A.K. Ojha, Designing vertically aligned porous $NiCo_2O_4$@$MnMoO_4$ Core@Shell nanostructures for high-performance asymmetric supercapacitors, J. Colloid Interface Sci. 580 (2020) 720–729, https://doi.org/10.1016/j. jcis.2020.07.062.

[38] M. Zhao, J. Deng, J. Liu, Y. Li, J. Liu, Z. Duan, J. Xiong, Z. Zhao, Y. Wei, W. Song, Y. Sun, Roles of surface-active oxygen species on 3DOM cobalt-based spinel catalysts $M_xCo_{3−x}O_4$ (M = Zn and Ni) for NO_x-assisted soot oxidation, ACS Catal. 9 (2019) 7548–7567, https://doi.org/10.1021/acscatal.9b01995.

[39] T. Wu, S. Sun, J. Song, S. Xi, Y. Du, B. Chen, W.A. Sasangka, H. Liao, C.L. Gan, G. G. Scherer, L. Zeng, H. Wang, H. Li, A. Grimaud, Z.J. Xu, Iron-facilitated dynamic active-site generation on spinel $CoAl_2O_4$ with self-termination of surface reconstruction for water oxidation, Nat. Catal. 2 (2019) 763–772, https://doi.org/ 10.1038/s41929-019-0325-4.

[40] S. Hung, Y. Hsu, C. Chang, C. Hsu, N. Suen, T. Chan, H.M. Chen, Unraveling geometrical site confinement in highly efficient iron-doped electrocatalysts toward oxygen evolution reaction, Adv. Energy Mater. 8 (2018) 1701686, https://doi.org/ 10.1002/aenm.201701686.

[41] W. Liu, C. Lu, K. Liang, B.K. Tay, A high-performance anode material for Li-ion batteries based on a vertically aligned CNTs/$NiCo_2O_4$ core/shell structure, Part. Part. Syst. Charact. 31 (2014) 1151–1157, https://doi.org/10.1002/ ppsc.201400030.

[42] Y. Zeng, Z. Lai, Y. Han, H. Zhang, S. Xie, X. Lu, Oxygen-vacancy and surface modulation of ultrathin nickel cobaltite nanosheets as a high-energy cathode for advanced Zn-ion batteries, Adv. Mater. 30 (2018) 1802396, https://doi.org/ 10.1002/adma.201802396.

[43] Y. Liu, Y. Ying, L. Fei, Y. Liu, Q. Hu, G. Zhang, S.Y. Pang, W. Lu, C.L. Mak, X. Luo, L. Zhou, M. Wei, H. Huang, Valence engineering via selective atomic substitution on tetrahedral sites in spinel oxide for highly enhanced oxygen evolution catalysis, J. Am. Chem. Soc. 141 (2019) 8136–8145, https://doi.org/10.1021/jacs.8b13701.

[44] Y. Liu, N. Zhang, C. Yu, L. Jiao, J. Chen, $MnFe_2O_4$@C nanofibers as high-performance anode for sodium-ion batteries, Nano Lett. 16 (2016) 3321–3328, https://doi.org/10.1021/acs.nanolett.6b00942.

[45] C. Chen, Y. Tuo, Q. Lu, H. Lu, S. Zhang, Y. Zhou, J. Zhang, Z. Liu, Z. Kang, X. Feng, de Chen, Hierarchical trimetallic Co-Ni-Fe oxides derived from core-shell structured metal-organic frameworks for highly efficient oxygen evolution reaction, Appl. Catal. B Environ. 287 (2021), 119953, https://doi.org/10.1016/j. apcatb.2021.119953.

[46] C. Guan, X. Liu, W. Ren, X. Li, C. Cheng, J. Wang, Rational design of metal-organic framework derived hollow $NiCo_2O_4$ arrays for flexible supercapacitor and electrocatalysis, Adv. Energy Mater. 7 (2017) 1602391, https://doi.org/10.1002/ aenm.201602391.

[47] T.M. Lima, V. de Macedo, D.S. Silva, W.N. Castelblanco, C.A. Pereira, R. E. Roncolatto, M.B. Gawande, R. Zbořil, R.S. Varma, E.A. Urquieta-González, Molybdenum-promoted cobalt supported on SBA-15: Steam and sulfur dioxide stable catalyst for CO oxidation, Appl. Catal. B Environ. 277 (2020), 119248, https://doi.org/10.1016/j.apcatb.2020.119248.

[48] M. Guo, Y. Liu, F. Zhang, F. Cheng, C. Cheng, Y. Miao, F. Gao, J. Yu, Inactive Al^{3+}-doped $La(CoCrFeMnNiAl_x)_{(1/(5+x))}O_3$ high-entropy perovskite oxides as high performance supercapacitor electrodes, J. Adv. Ceram. 11 (2022) 742–753, https://doi.org/10.1007/s40145-022-0568-4.

[49] J. Yang, C. Yu, S. Liang, S. Li, H. Huang, X. Han, C. Zhao, X. Song, C. Hao, P. M. Ajayan, J. Qiu, Bridging of ultrathin $NiCo_2O_4$ nanosheets and graphene with polyaniline: a theoretical and experimental study, Chem. Mater. 28 (2016) 5855–5863, https://doi.org/10.1021/acs.chemmater.6b02303.

[50] C. Yuan, J. Li, L. Hou, X. Zhang, L. Shen, X.W.D. Lou, Ultrathin mesoporous $NiCo_2O_4$ nanosheets supported on Ni foam as advanced electrodes for supercapacitors, Adv. Funct. Mater. 22 (2012) 4592–4597, https://doi.org/ 10.1002/adfm.201200994.

[51] X. Shan, J. Liu, H. Mu, Y. Xiao, B. Mei, W. Liu, G. Lin, Z. Jiang, L. Wen, L. Jiang, An engineered superhydrophilic/superaerophobic electrocatalyst composed of the supported $CoMoS_x$ chalcogel for overall water splitting, Angew. Chem. Int. Ed. 59 (2020) 1659–1665, https://doi.org/10.1002/anie.201911617.

[52] Y. He, Y. Cui, W. Shang, Z. Zhao, P. Tan, Insight into the bubble-induced overpotential towards high-rate charging of Zn-air batteries, Chem. Eng. J. 448 (2022), 137782, https://doi.org/10.1016/j.cej.2022.137782.

[53] G.B. Darband, M. Aliofkhazraei, S. Shanmugam, Recent advances in methods and technologies for enhancing bubble detachment during electrochemical water splitting, Renew. Sust. Energ. Rev. 114 (2019), 109300, https://doi.org/10.1016/j. rser.2019.109300.

[54] Y. He, Y. Cui, Z. Zhao, Y. Chen, W. Shang, P. Tan, Strategies for bubble removal in electrochemical systems, Energy Rev. 2 (2023), 100015, https://doi.org/10.1016/ j.enrev.2023.100015.

[55] K.-L. Yan, X. Shang, Z. Li, B. Dong, X. Li, W.-K. Gao, J.-Q. Chi, Y.-M. Chai, C.-G. Liu, Ternary mixed metal Fe-doped $NiCo_2O_4$ nanowires as efficient electrocatalysts for oxygen evolution reaction, Appl. Surf. Sci. 416 (2017) 371–378, https://doi.org/ 10.1016/j.apsusc.2017.04.204.

[56] P. Wu, J. Wu, H. Si, Z. Zhang, Q. Liao, X. Wang, F. Dai, K. Ammarah, Z. Kang, Y. Zhang, 3D Holey-graphene architecture expedites ion transport kinetics to push the OER performance, Adv. Energy Mater. 10 (2020) 2001005, https://doi.org/ 10.1002/aenm.202001005.

[57] M.A. Kazakova, D.M. Morales, C. Andronescu, K. Elumeeva, A.G. Selyutin, A. V. Ishchenko, G.V. Golubtsov, S. Dieckhöfer, W. Schuhmann, J. Masa, Fe/Co/Ni mixed oxide nanoparticles supported on oxidized multi-walled carbon nanotubes as electrocatalysts for the oxygen reduction and the oxygen evolution reactions in alkaline media, Catal. Today 357 (2020) 259–268, https://doi.org/10.1016/j. cattod.2019.02.047.

[58] D.M. Morales, M.A. Kazakova, S. Dieckhöfer, A.G. Selyutin, G.V. Golubtsov, W. Schuhmann, J. Masa, Trimetallic Mn-Fe-Ni oxide nanoparticles supported on multi-walled carbon nanotubes as high-performance bifunctional ORR/OER electrocatalyst in alkaline media, Adv. Funct. Mater. 30 (2020) 1905992, https:// doi.org/10.1002/adfm.201905992.

[59] F.-T. Tsai, Y.-T. Deng, C.-W. Pao, J.-L. Chen, J.-F. Lee, K.-T. Lai, W.-F. Liaw, The HER/OER mechanistic study of an FeCoNi-based electrocatalyst for alkaline water splitting, J. Mater. Chem. A 8 (2020) 9939–9950, https://doi.org/10.1039/D0TA01877E.

[60] X. Liu, R. Guo, K. Ni, F. Xia, C. Niu, B. Wen, J. Meng, P. Wu, J. Wu, X. Wu, L. Mai, Reconstruction-determined alkaline water electrolysis at industrial temperatures, Adv. Mater. 32 (2020) 2001136, https://doi.org/10.1002/adma.202001136.

[61] X. Guo, X. Hu, D. Wu, C. Jing, W. Liu, Z. Ren, Q. Zhao, X. Jiang, C. Xu, Y. Zhang, N. Hu, Tuning the bifunctional oxygen electrocatalytic properties of core-shell Co3O4@NiFe LDH Catalysts for Zn-air batteries: effects of interfacial cation valences, ACS Appl. Mater. Interfaces 11 (2019) 21506–21514, https://doi.org/10.1021/acsami.9b04217.

[62] M.S. Kim, M.H. Naveen, R. Khan, J.H. Bang, Iterative oxidation and sulfidation reactions: revival of bulk cobalt sulfide into an active electrocatalyst for the oxygen evolution reaction, J. Mater. Chem. A 8 (2020) 7647–7652, https://doi.org/10.1039/D0TA01578D.

[63] K. Karuppasamy, R. Bose, D. Vikraman, S. Ramesh, H.S. Kim, E. Alhseinat, A. Alfantazi, H.-S. Kim, Revealing the effect of various organic ligands on the OER activity of MOF-derived 3D hierarchical cobalt oxide @ carbon nanostructures, J. Alloy. Compd. 934 (2023), 167909, https://doi.org/10.1016/j.jallcom.2022.167909.

[64] H. Zhao, H. Yao, S. Wang, Y. Cao, Z. Lu, J. Xie, J. Hu, A. Hao, Doping-engineered bifunctional oxygen electrocatalyst with Se/Fe-doped Co3O4/N-doped carbon nanosheets as highly efficient rechargeable zinc-air batteries, J. Colloid Interface Sci. 626 (2022) 475–485, https://doi.org/10.1016/j.jcis.2022.06.147.

[65] W. Song, Z. Ren, S.-Y. Chen, Y. Meng, S. Biswas, P. Nandi, H.A. Elsen, P.-X. Gao, S. L. Suib, Ni- and Mn-promoted mesoporous Co3O4: a stable bifunctional catalyst with surface-structure-dependent activity for oxygen reduction reaction and oxygen evolution reaction, ACS Appl. Mater. Interfaces 8 (2016) 20802–20813, https://doi.org/10.1021/acsami.6b06103.

[66] H. Wang, S. Hung, H. Chen, T. Chan, H.M. Chen, B. Liu, In operando identification of geometrical-site-dependent water oxidation activity of spinel Co3O4, J. Am. Chem. Soc. 138 (2016) 36–39, https://doi.org/10.1021/jacs.5b10525.

[67] A. Moysiadou, S. Lee, C.-S. Hsu, H.M. Chen, X. Hu, Mechanism of oxygen evolution catalyzed by cobalt oxyhydroxide: cobalt superoxide species as a key intermediate and dioxygen release as a rate-determining step, J. Am. Chem. Soc. 142 (2020) 11901–11914, https://doi.org/10.1021/jacs.0c04867.

[68] Y. Zhang, H. Guo, P. Yuan, K. Pang, B. Cao, X. Wu, L. Zheng, R. Song, Structural evolution of CoMoO4 to CoOOH by ion electrochemical etching for boosting oxygen evolution reaction, J. Power Sources 442 (2019), 227252, https://doi.org/10.1016/j.jpowsour.2019.227252.

[69] S. Wang, W. Huo, F. Fang, Z. Xie, J.K. Shang, J. Jiang, High entropy alloy/C nanoparticles derived from polymetallic MOF as promising electrocatalysts for alkaline oxygen evolution reaction, Chem. Eng. J. 429 (2022), 132410, https://doi.org/10.1016/j.cej.2021.132410.

[70] N. Kornienko, N. Heidary, G. Cibin, E. Reisner, Catalysis by design: development of a bifunctional water splitting catalyst through an operando measurement directed optimization cycle, Chem. Sci. 9 (2018) 5322–5333, https://doi.org/10.1039/c8sc01415a.

[71] E. Budiyanto, S. Salamon, Y. Wang, H. Wende, H. Tüysüz, Phase segregation in cobalt iron oxide nanowires toward enhanced oxygen evolution reaction activity, JACS Au 2 (2022) 697–710, https://doi.org/10.1021/jacsau.1c00561.

[72] J. Huang, H. Sheng, R.D. Ross, J. Han, X. Wang, B. Song, S. Jin, Modifying redox properties and local bonding of Co3O4 by CeO2 enhances oxygen evolution catalysis in acid, Nat. Commun. 12 (2021) 3036, https://doi.org/10.1038/s41467-021-23390-8.

[73] W. Chen, B. Wu, Y. Wang, W. Zhou, Y. Li, T. Liu, C. Xie, L. Xu, S. Du, M. Song, D. Wang, Y. liu, Y. Li, J. Liu, Y. Zou, R. Chen, C. Chen, J. Zheng, Y. Li, J. Chen, S. Wang, Deciphering the alternating synergy between interlayer Pt single-atom and NiFe layered double hydroxide for overall water splitting, Energy Environ. Sci. 14 (2021) 6428–6440, https://doi.org/10.1039/D1EE01395E.

[74] M.H. Naveen, T.L. Bui, L. Lee, R. Khan, W. Chung, R. Thota, S.-W. Joo, J.H. Bang, Nanostructuring matters: stabilization of electrocatalytic oxygen evolution reaction activity of ZnCo2O4 by zinc leaching, ACS Appl. Mater. Interfaces 14 (2022) 15165–15175, https://doi.org/10.1021/acsami.1c24403.

[75] J. Chen, H. Li, Z. Yu, C. Liu, Z. Yuan, C. Wang, S. Zhao, G. Henkelman, S. Li, L. Wei, Y. Chen, Octahedral coordinated trivalent cobalt enriched multimetal oxygen-evolution catalysts, Adv. Energy Mater. 10 (2020) 2002593, https://doi.org/10.1002/aenm.202002593.

[76] Z. Xiao, Y.-C. Huang, C.-L. Dong, C. Xie, Z. Liu, S. Du, W. Chen, D. Yan, L. Tao, Z. Shu, G. Zhang, H. Duan, Y. Wang, Y. Zou, R. Chen, S. Wang, Operando identification of the dynamic behavior of oxygen vacancy-rich Co3O4 for oxygen evolution reaction, J. Am. Chem. Soc. 142 (2020) 12087–12095, https://doi.org/10.1021/jacs.0c00257.

[77] S. Peng, F. Gong, L. Li, D. Yu, D. Ji, T. Zhang, Z. Hu, Z. Zhang, S. Chou, Y. Du, S. Ramakrishna, Necklace-like multishelled hollow spinel oxides with oxygen vacancies for efficient water electrolysis, J. Am. Chem. Soc. 140 (2018) 13644–13653, https://doi.org/10.1021/jacs.8b05134.

[78] G.S. Hutchings, Y. Zhang, J. Li, B.T. Yonemoto, X. Zhou, K. Zhu, F. Jiao, In situ formation of cobalt oxide nanocubanes as efficient oxygen evolution catalysts, J. Am. Chem. Soc. 137 (2015) 4223–4229, https://doi.org/10.1021/jacs.5b01006.

[79] Z. Xu, Y. Wu, Q. Ji, T. Li, C. Xu, C. Qi, H. He, S. Yang, S. Li, S. Yan, C. Sun, L. Zhang, Z. Zou, Understanding spatial effects of tetrahedral and octahedral cobalt cations on peroxymonosulfate activation for efficient pollution degradation, Appl. Catal. B Environ. 291 (2021), 120072, https://doi.org/10.1016/j.apcatb.2021.120072.

[80] X. Chen, Q. Wang, Y. Cheng, H. Xing, J. Li, X. Zhu, L. Ma, Y. Li, D. Liu, S-doping triggers redox reactivities of both iron and lattice oxygen in FeOOH for low-cost and high-performance water oxidation, Adv. Funct. Mater. 32 (2022) 2112674, https://doi.org/10.1002/adfm.202112674.

[81] T. Kim, S.B. Roy, S. Moon, S. Yoo, H. Choi, V.G. Parale, Y. Kim, J. Lee, S.C. Jun, K. Kang, S.-H. Chun, K. Kanamori, H.-H. Park, Highly dispersed Pt clusters on F-doped tin(IV) oxide aerogel matrix: an ultra-robust hybrid catalyst for enhanced hydrogen evolution, ACS Nano 16 (2022) 1625–1638, https://doi.org/10.1021/acsnano.1c10504.

[82] C.G. Morales-Guio, L. Liardet, X. Hu, Oxidatively electrodeposited thin-film transition metal (oxy)hydroxides as oxygen evolution catalysts, J. Am. Chem. Soc. 138 (2016) 8946–8957, https://doi.org/10.1021/jacs.6b05196.